Quasi-Deterministic Channel Model Parameters for a Data Center at 60 GHz

Camillo Gentile, Peter B. Papazian, Ruoyu Sun, Jelena Senic, and Jian Wang

***Abstract*—We describe a measurement campaign conducted in a data center, a unique environment in which transceivers are positioned above the server racks. A total of 80 channel acquisitions, including small-scale measurements, were recorded using our three-dimensional double-directional 60 GHz channel sounder with 0.5 ns delay resolution and 2° average angle error. For each acquisition, the channel multipath components were extracted in the delay-angle space and subsequently reduced to the parameters of the Quasi-Deterministic channel model: a stochastic map-based model that represents the scattering of incident waves off ambient reflectors as specular components, each surrounded by a cluster of diffuse components. The weaker diffuse components interfere with the stronger specular component, giving rise to small-scale fading. Only with super-resolution capabilities, such as that of our system, were we able to show how densely the diffuse components were packed, with 1/ns to 2/ns arrival rates and cluster angular spreads between 3° and 4°. Most importantly, we measured the diffuse power to be as high as 26% of the total cluster power, demonstrating that small-scale fading at millimeter-wave frequencies can be significant.**

***Index Terms*—Millimeter-wave (mmWave), server room, wireless.**

I. Introduction

Fifth generation (5G) is more than a simple shift in frequency to millimeter-wave (mmWave) bands. In fact, even before 4G, there was a significant channel-modeling effort to characterize the 60 GHz band after its unlicensing in 2001 [1], [2]. The real game-changer for 5G has been the development of mmWave phased-array antennas whose high gain can compensate for the much greater path loss in these bands, enabling link distances up to hundreds of meters for mobile communications. To do so, the transmitter (TX) and receiver (RX) will steer their beams toward the respective angle-of-departure (AoD) and angle-of-arrival (AoA) viable propagation paths between the two. Hence, 5G channel models must capture the double-directionality of the channel.

The easiest approach to achieve this has been to equip channel sounders with directional horns that are swept in angle using mechanical rotation [3]–[8]. The angles, however, are not resolvable beyond the beamwidth of the antennas, which are typically 10°–20°. More advanced approaches mechanically translate the antennas on positioners to enable coherent combining for super-resolution in angle [9]. The drawback of these systems is that they are notoriously slow and a single channel acquisition can take up to 6 h, typically limiting measurement campaigns to tens of acquisitions. Moreover, the systems cannot deal with mobile scenarios or other time-variant impulse responses, for which small-scale fading and Doppler spread become relevant.

The source of small-scaling fading—multipath interference over the order of wavelengths—for 5G is very different than its predecessors. At lower frequencies, the channel is rich in multipath due to the presence of both diffraction and reflection. In addition, the omnidirectional antenna at the mobile station will capture all paths, exacerbating the interference. Finally, the ability to resolve individual paths is diminished as bandwidths are orders of magnitude less than 5G. On the contrary, at mmWave frequencies, diffraction is much weaker than reflection [10], rendering the channel "sparse." Rather, diffuse reflections from surface roughness must now be accounted for since the roughness is comparable in size to the wavelength. Weaker diffuse reflections cluster around the stronger specular reflections in the delay-angle space, and so when the transceivers steer their beams towards the specular paths, they will inevitably detect diffuse components as well, giving rise to fading.

We are aware of three efforts to date to characterize mmWave fading with measurements. In [11], solely delay-domain statistics, with 4 ns delay resolution, were provided because the sounder has no directional capabilities; hence, complementary ray-tracing simulations were conducted. Although the system in [6] has double-directionality, the delay resolution is just 2.5 ns and the angular resolution just 11°; moreover, no small-scale measurements were taken, and so the fading model was based on the large-scale statistics. The only system that takes actual small-scale measurements, with 0.25 ns resolution, is the one described earlier in [9]; however, because of the long acquisition time, the system was reconfigured as in [12] without coherent combination, reverting the angular resolution to the 15° and 30° beamwidths of the two antennas used. The fundamental problem with these measurements is that most lack sufficient delay resolution and none have sufficient angular resolution to characterize diffuse components, which are dense in nature.

For example, we observed multipath arrival rates between 1/ns and 2/ns and cluster angle spreads between 3° and 4°. Besides to characterize fading, angular spread has a one-to-one mapping to Doppler spread [13]. Our experimental data shows that in some measurements the diffuse power was as high as 26% of the total cluster power; hence, it cannot be neglected. These observations were made using our state-of-the-art 60 GHz channel sounder with 0.5 ns delay resolution [14]. The 16 × 8 system implements coherent combining between antennas to provide super-resolution in three-dimensional (3-D)

Manuscript received January 23, 2018; revised March 2, 2018, March 13, 2018, and March 14, 2018; accepted March 15, 2018. Date of publication March 19, 2018; date of current version May 3, 2018. *(Corresponding author: Camillo Gentile.)*

The authors are with the Communications Technology Laboratory, National Institute of Standards and Technology, Gaithersburg, MD 20899 USA (e-mail: camillo.gentile@nist.gov; peter.papazian@nist.gov; ruoyu.sun@nist.gov; jelena.senic@nist.gov; jian.wang@nist.gov).

Digital Object Identifier 10.1109/LAWP.2018.2817066

AoD and AoA, with average angular error around 2°. Most critically, the sweep period of our system is only 262 μs, well within the channel coherence time. This enables taking multiple small-scale acquisitions in just milliseconds; moreover, mobile channels up to 35 km/h closing speed can be sounded.

In this letter, the parameters of the Quasi-Deterministic (QD) channel model [11] were reduced from measurements in a data center. The stochastic map-based model accounts for scattering of multipath components (MPCs) from ambient reflectors, enabling accurate reconstruction of the channel impulse response in the delay-angle space, essential for the proper design of mmWave communications systems. The main contributions of our work are listed as follows:

1) 3-D double-directional channel measurements in a data center at mmWave frequencies, for a total of 80 channel acquisitions including small-scale measurements;
2) validation of the map-based properties against a 2-D map of the environment and validation of the stochastic properties through the curve-fitting residual error;
3) delay- and angle-dispersion characteristics of the channel characterizing small-scale fading at mmWave frequencies.

II. Data-Center Use Case

The IEEE 802.11ay amendment [15] operating in the 60 GHz unlicensed band is expected for release in 2018. It will support up to eight data streams through spatial multiplexing, yielding a total throughput of 100 Gb/s. Use cases for 802.11ay [16] include wireless backup in a data center. In this unique propagation environment, transceivers are positioned above the server racks and in turn close to the ceiling; given the height of the racks, human presence can be neglected. Besides the direct path, racktop and ceiling bounces as well as any other strong paths within the constrained field-of-view of the transceivers (above the racks) can be exploited for spatial multiplexing.

The use case, however, is not unique to 802.11ay and has been growing in interest over the past five years given the exponential growth of cloud services. Yet, little experimental data is available to date. In [17] and [18], wireless testbeds to evaluate connectivity and throughput using 3-D beamforming in a data center are described, but only received signal strength is measured in terms of the channel metrics. To our knowledge, [19] is the only paper—a very recent one—to collect propagation measurements in a data center with an actual channel sounder. However, lacking directional antennas, the angular properties of the channel are not characterized and only path-loss models and rms delay statistics are reported.

III. Channel Measurements

A. Channel Sounder

Fig. 1 displays the TX and RX arrays of our 60 GHz channel sounder. Schematics of the RF front ends can be found in [20]. The TX features a semicircular array of eight horn antennas, each with 18.1 dBi gain and 22.5° beamwidth. To avoid "blind spots," the angular spacing between the elements matches the beamwidth of the horns; specifically, the elements are spaced at 22.5° horizontally, and vertically adjacent elements are pointed outwards at 0° and upwards at 22.5°. Consequently, the horizontal beamwidth of the array is 180° and its vertical beamwidth is 45°. The 3-D spatial diversity enables characterizing AoD in both azimuth and elevation. The RX features two semicircular arrays to estimate AoA—each one is a replica of the TX array—extending the horizontal beamwidth of the array to an omnidirectional view, essential for mobile scenarios.

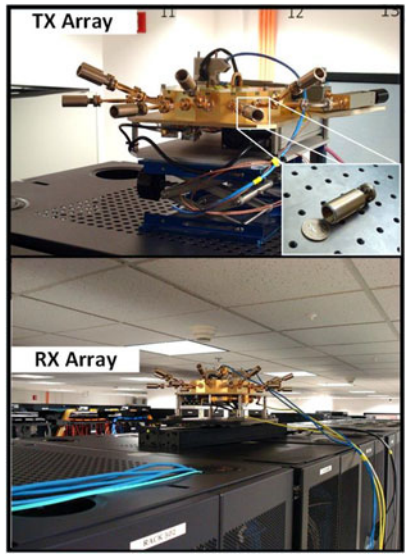

Fig. 1. TX antenna array of our 60 GHz channel sounder mounted on a fixed labjack and RX antenna array mounted on a single-axis positioner. Their field-of-view above the racks can be observed.

The system transmits a repeating 2047 bit pseudorandom (PN) codeword that has a chip rate of 2 GHz. With precision synchronization using Rubidium clocks, all the TX and RX elements are switched pairwise. A channel acquisition consisting of a full sweep of the 128 (16×8) pairs requires 262 μs. The codeword is generated at IF and then upconverted to 60.5 GHz. At the RX, the received signal is downconverted back to IF and then digitized at 40 G samples/s. For each pair, the received signal is correlated with the known PN codeword to generate a complex channel impulse response. The maximum measurable dynamic range of the system is 162 dB.

Given the antenna centers of the TX- and RX-array elements, the 128 channel impulse responses from a measurement were coherently combined through the SAGE algorithm to extract the channel MPCs [21]. The antennas patterns were de-embedded through the SAGE algorithm, and the responses of the TX and RX front ends were removed through predistortion filters designed from the back-to-back calibration method [14]. Hence, the properties of the MPCs reflect the pure response of the channel alone and not the measurement system.

B. Measurement Campaign

The measurement campaign was conducted in an 18×18 m^2 data center. Its 2-D map is displayed in Fig. 2(a) as well as the azimuth coordinate system for AoA and AoD. The ceiling height is 2.56 m, and the rack height varied between 1.96 and 2.00 m. An air curtain—typical of data centers—was found next to the supercomputers; made from conductive material, it serves to concentrate cooling such that heat is dissipated more efficiently. Due to movement of the curtain caused by strong airflow, we observed time-variant impulse responses.

In our campaign, there was a single TX location and ten large-scale RX locations. As a guideline for the equipment setup, we followed the IEEE 802.11ay data center usage case

(a)

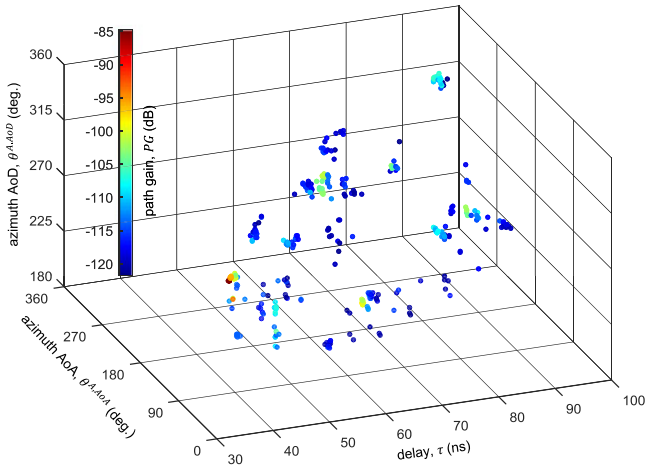

(b)

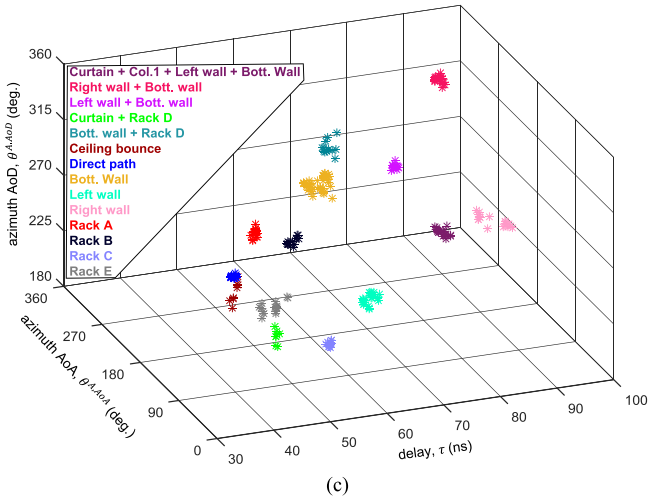

(c)

Fig. 2. (a) 2-D map of data center. The grid size is 1×1 m^2. The TX and RX were placed on top of the racks (shaded in pink). The MPCs in (c) were projected onto the map, revealing the locations of the MPC reflection points. The same color scheme in the legend of (c) was used. (b) MPCs detected in acquisitions for RX6, each indexed according to delay, azimuth AoD, and azimuth AoA. Path gain is color-coded against legend. (c) Clustered multipath components for RX6. Each cluster is displayed as a different color and is labeled in reference to the reflector(s) in (a) that generated it.

in [16]: the transceivers were placed on the racktops, and both intra-rack (RX1–RX3) and inter-rack (RX4–RX10) scenarios were considered. The TX was stationary and mounted on a labjack (pictured in Fig. 1). The RX array, on the other hand, was mounted on a single-axis positioner (also shown in Fig. 1). The positioner collected eight small-scale acquisitions spaced at 5 mm (one wavelength) apart for each large-scale RX location, for a total of 80 channel acquisitions. The antenna centers of the outward TX and RX elements were aligned at 19 cm above the racktop using a laser pointer.

IV. Quasi-Deterministic Channel Model

The IEEE 802.11ay task group as well as other industry consortia (e.g., METIS, MiWEBA, and mmMAGIC) have subscribed to map-based channel models for mmWave systems, of which the QD model has become the benchmark. In the QD model, the direct path and reflected paths only are considered, as diffraction has been shown to be insignificant at mmWave bands [10]. The direct path is completely deterministic: Its delay, AoD, and AoA are computed from the geometry of the TX and RX, and its path gain in line-of-sight from the Friis transmission equation. Similarly, specular reflections are also deterministic, given the map of the environment and any reflection loss. Each specular reflection gives rise to scattering of the incident wave into a strong specular MPC—also known as a *cursor*—and weaker diffuse components that *cluster* around the cursor. The diffuse reflections stem from surface roughness that is comparable to the size of the wavelength at mmWave frequencies. The nondeterministic property of the model concerns the small-scale dispersion statistics of the clustered scattering. In the sequel, we describe the QD parameters and our approach to fit them to the measurements.

A. MPC Clustering and QD Parameter Fitting

The MPCs extracted from a single acquisition were indexed by path gain (PG), delay (τ), and azimuth and elevation AoD $(\theta^{A,\mathrm{AoD}}, \theta^{E,\mathrm{AoD}})$ and AoA $(\theta^{A,\mathrm{AoA}}, \theta^{E,\mathrm{AoA}})$. (The azimuth and elevation of the AoA and AoD were validated with a mean error of 2.1° [14].) As an illustrative example, Fig. 2(b) shows the MPCs for RX6. Once extracted, the paths were clustered in the delay, AoD, and AoA dimensions through the algorithm in [21]. An underlying principle of the algorithm is that each cluster has a single peak originating from a specular reflection. Fig. 2(c) shows the clustering of the MPCs. Note that some of the original components in Fig. 2(b) were discarded through density filtering: a preliminary stage of the algorithm targeting weak MPCs isolated in space, usually corresponding to diffracted paths.

Following the clustering step, the QD parameters of each cluster were fit to the data. Each cluster identified had N MPCs indexed through i. First, the RMS spreads for each of the four angles were computed as

$$\sigma_\theta^{A/E,\mathrm{AoD/AoA}} = \sqrt{\frac{\sum_{i=1}^{N} \mathrm{PG}_i \left(\theta_i^{A/E,\mathrm{AoD/AoA}} - \mu_\theta\right)^2}{\sum_{i=1}^{N} \mathrm{PG}_i}}$$

$$\mu_\theta = \frac{\sum_{i=1}^{N} \mathrm{PG}_i \theta_i^{A/E,\mathrm{AoD/AoA}}}{\sum_{i=1}^{N} \mathrm{PG}_i}. \quad (1)$$

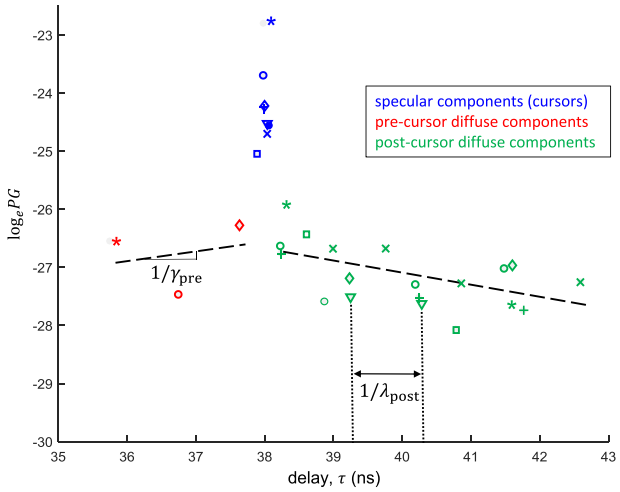

Fig. 3. Multipath components of a typical cluster aggregated over eight small-scale measurements (each displayed with a different symbol). Note that the ordinate was plotted as $\log_e \mathrm{PG}$, converting (4) from exponential to linear.

Next, for each cluster, the cursor was identified as the cluster peak, i.e., the MPC in the cluster with the highest path gain, $\mathrm{PG}_{\text{cursor}}$. The cursor path gain is given by the free-space gain, $\mathrm{PG}_{\mathrm{FS}}$, multiplied by the reflection gain RG due to incidence of the plane wave with the reflector, or $\mathrm{PG}_{\text{cursor}} = \mathrm{PG}_{\mathrm{FS}}\mathrm{RG}$. Given the delay of the cursor τ_{cursor}, the free-space gain is computed from the Friis transmission equation as $\mathrm{PG}_{\mathrm{FS}} = (\frac{1}{4\pi f_c \tau_{\text{cursor}}})^2$. Then, the reflection-loss parameter of the QD model can be computed as

$$\mathrm{RL} = \frac{1}{\mathrm{PG}} = \frac{1}{\mathrm{PG}_{\text{cursor}}(4\pi f_c \tau_{\text{cursor}})^2}. \tag{2}$$

With the cursor identified, the remaining diffuse components within the cluster were partitioned along the delay dimension into two segments: N_{pre} pre-cursor MPCs arriving before the cursor and N_{post} post-cursor MPCs arriving after, where $N = N_{\text{pre}} + N_{\text{post}} + 1$. Fig. 3 shows measurements for a typical cluster. The relative strength of the cursor with respect to pre-cursor or post-cursor diffuse components is gauged through the *K*-factor as

$$K_{\text{pre/post}} = \frac{\mathrm{PG}_{\text{cursor}}}{\sum_{i=1}^{N_{\text{pre/post}}} \mathrm{PG}_i}. \tag{3}$$

The pre-cursor and post-cursor components then rise and fall according to

$$\begin{aligned} \mathrm{PG}_{\text{pre}}(\tau) &= \frac{\mathrm{PG}_{\text{cursor}}}{K_{\text{pre}}} e^{\frac{(\tau-\tau_{\text{cursor}})}{\gamma_{\text{pre}}} + S_{\text{pre}}} \\ \mathrm{PG}_{\text{post}}(\tau) &= \frac{\mathrm{PG}_{\text{cursor}}}{K_{\text{post}}} e^{-\frac{(\tau-\tau_{\text{cursor}})}{\gamma_{\text{post}}} + S_{\text{post}}} \end{aligned} \tag{4}$$

where γ is known as the decay constant determined through a least-squares fit to the extracted MPCs and $S \sim \mathcal{N}(0, \sigma_S)$ is the residual error. Finally, intra-cluster arrival delays are characterized by exponential probability density function

$$f_{\text{post/pre}}(\tau_i|\tau_{i-1}) \sim \lambda_{\text{post/pre}} e^{-\lambda_{\text{post/pre}}(\tau_i - \tau_{i-1})} \tag{5}$$

where λ is the known as the arrival rate.

To capture the delay- and angle-dispersion fading characteristics, the MPCs from the eight small-scale measurements were aggregated for clustering and parameter fitting. In Fig. 3, each measurement is displayed with a different symbol. Because the measurements were taken a wavelength apart, the scattering is known to be independent. This supplied over 30 data points per cluster for robust statistical characterization.

B. Cluster Classification

The clustered MPCs were projected from the multidimensional delay-angle space onto the coordinate system of the 2-D map through the equations in [23], equivalent to inverse ray-tracing. Fig. 2(a) shows the projection from Fig. 2(c) for RX6, maintaining the same color scheme as in the legend. For the direct path, the coordinates correspond to the estimated position of the RX, while for the first-order reflections they correspond to the estimated reflection points. Reflections above first order were not shown to reduce clutter. The reflection points reveal the locations of the reflectors, from which the clusters could be classified. Agreement between the locations of the reflectors in the floorplan and the delay-angle properties of the cursors is clear. Note that the clustered diffuse components from any reflector were between 1 and 3 m apart.

While reflections up to fourth order were detected, in this letter, we only report on single-order reflectors for two reasons: 1) together, the MPCs associated with the direct path and single-order reflections accounted for over 99.5% of the total energy detected; 2) this simplified the model, avoiding the enumeration of all permutations of the multiple-order reflectors in the environment while preserving accuracy.

V. Results

Across the ten RX locations, the measured gain for the direct path fell within 1.2 dB of the theoretical value $\mathrm{PG}_{\mathrm{FS}}$. Because the direct path is not scattered, there are no clustering properties associated with it. For the single-order reflections, Table I lists the mean μ and standard deviation σ of the QD parameters for five main reflector classes observed within the field-of-view of the transceivers. The model parameters were derived from a total of 52 single-order clusters identified. The mean standard deviation of the residual error μ_{σ_S} never exceeded 3 dB, meaning the measured data fit the channel model very well.

For the conductive air curtain, the mean reflection loss was $\mu_{\mathrm{RL}} = 0.1$ dB, so it behaved as a minimum-loss source for multipath in the environment, generating exploitable paths for beamforming. The mild ridges in the curtain generated post-cursor diffuse components, whereas the pre-cursor activity was negligible. The bounce from the acoustic ceiling tiles also provided a relatively strong ($\mu_{\mathrm{RL}} = 7.6$ dB) reliable alternative to the direct path; the pre-cursor activity was negligible for the ceiling, but even the post-cursor diffuse components were weak, as evidenced by $\mu_{K_{\text{post}}} = 12.4$ dB, much larger than for the other reflectors.

Although the ceiling bounce occurred at 37 cm above the TX-RX plane, it could be clearly resolved from the direct path. This was not the case for the racktop bounce 19 cm below the plane, which was combined with the direct-path pulse, necessitating super-resolution techniques to deconvolve it. For example, at RX1, the ceiling bounce arrived within 0.22 ns and 10.0° elevation AoD/AoA of the direct path, while the racktop

TABLE I
QD MODEL PARAMETER VALUES FOR SINGLE-ORDER REFLECTORS

	K (dB)				γ (ns)				σ_S (dB)		$\lambda\,(1/\mathrm{ns})$				σ_θ (deg.)**		RL (dB)	
	Pre		Post		Pre		Post		Pre	Post	Pre		Post					
Reflector	μ	σ	μ	σ	μ	σ	μ	σ	μ	μ	μ	σ	μ	σ	μ	σ	μ	σ
Ceiling			12.4	6.2			0.74	0.53		1.18			1.93	1.96	2.6	1.6	7.6	2.6
Racktop*																	6.8	1.1
Curtain			7.3	4.4			0.95	0.59	1.88	2.29			1.17	0.34	3.6	1.2	0.1	1.2
Wall/Column	8.4	6.2	7.9	3.7	0.37	0.52	0.89	0.70	2.85	2.48	8.4	6.2	1.41	1.06	3.1	1.6	7.2	1.4
Rackside	8.5	4.6	6.9	4.8	2.50	3.51	3.52	2.02	2.99	1.50	8.5	4.6	1.14	1.15	3.8	1.4	15.9	4.3

*Only valid for intra-rack configuration RX1-RX3.
**Averaged over all four $\theta^{A/E,\mathrm{AoD/AoA}}$.

bounce arrived within 0.06 ns and 5.2° elevation AoD/AoA. Notice that the racktop bounce only existed for the three RX positions on the same racktop as the TX, RX1-RX3. No significant scattering was observed from the racktop, i.e., the cluster was composed from the cursor alone; therefore, we only reported on the reflection loss.

Bounces from the sides of the racks were not from specular reflections because the racks lay below the TX-RX plane. It follows that any reflected components from the rack sides were diffuse—one side has meshed doors while the reverse side was laden with server equipment and thick cabling—which is why $\mu_{\mathrm{RL}} = 15.9$ dB is so large. The decay constants were also very large compared to the other reflectors due their roughness and elongated scattering plane. Most rackside bounces were traced to adjacent racks, but some were traced to racks as far as two rows over. Although they were significantly weaker than the other bounces, they must be considered as potential interferers. The two columns and the four walls were all covered with drywall, and so were grouped into the same class. They also represented a consistent set of reflectors with relatively low loss ($\mu_{\mathrm{RL}} = 7.2$ dB).

The arrival rate of the multipath within the clusters ranged between 1/ns and 2/ns, and the angular spread of the clusters between 3° and 4°. Most importantly, we show that the percentage of diffuse power to the total power of the cluster, computed as $(\frac{1}{K^{\mathrm{pre}}} + \frac{1}{K^{\mathrm{post}}})/(1 + \frac{1}{K^{\mathrm{pre}}} + \frac{1}{K^{\mathrm{post}}})$, can be as high as 26%. This means that the diffuse components, which interfere with the main specular component to generate small-scale fading, cannot be neglected in the design of mmWave systems.

REFERENCES

[1] N. Moraitis and P. Constantinou, "Indoor channel measurements and characterization at 60 GHz for wireless local area network applications," *IEEE Trans. Antennas Propag.*, vol. 52, no. 12, pp. 3180–3189, Dec. 2004.

[2] T. Zwick, T.J. Beukema, and H. Nam, "Wideband channel sounder with measurements and model for the 60 GHz indoor radio channel," *IEEE Trans. Veh. Technol.*, vol. 54, no. 4, pp. 1266–1277, Jul. 2005.

[3] A. Maltsev *et al.*, "Experimental Investigations of 60 GHz WLAN systems in office environments," *IEEE J. Sel. Areas Commun.*, vol. 27, no. 8, pp. 1266–1277, Oct. 2009.

[4] H. Sawada *et al.*, "Impulse response model and parameters for indoor channel modeling at 60 GHz," in *Proc. IEEE 71st Veh. Technol. Conf.*, May 2010, pp. 1–5.

[5] S. Hur *et al.*, "Synchronous channel sounder using horn antenna and indoor measurements on 28 GHz," in *Proc. IEEE Black Sea Conf.*, May 2014, pp. 1–5.

[6] M. F. Akdeniz *et al.*, "Millimeter wave channel modeling and cellular capacity evaluation," *IEEE J. Sel. Areas Commun.*, vol. 32, no. 6, pp. 1164–1179, Jun. 2014.

[7] J.-J. Park *et al.*, "Millimeter-wave channel model parameters for urban microcellular environment based on 28 and 38 GHz measurements," in *Proc. IEEE Symp. Personal, Indoor, Mobile Radio Commun.*, Sep. 2016.

[8] B.N. Lia and D. G. Michelson, "Characterization of multipath persistence in device-to-device scenarios at 30 GHz," in *Proc. IEEE Global Commun. Conf.*, Dec. 2016, pp. 1–6.

[9] D. Dupleich *et al.*, "A hybrid polarimetric wide-band beam-former architecture for 5G mm-wave communications," in *Proc. IEEE Workshop Smart Antennas*, Mar. 2016, pp. 1–8.

[10] J. Senic *et al.*, "Analysis of E-band Path loss and propagation mechanisms in the indoor environment," *IEEE Trans. Antennas Propag.*, vol. 65, no. 12, pp. 6562–6573, Dec. 2017.

[11] A. Maltsev *et al.*, "Quasi-deterministic approach to mmWave channel modeling in a non-stationary environment," in *Proc. IEEE Global Commun. Conf.*, pp. 1–6, Dec. 2014.

[12] N. Iqbal *et al.*, "Modeling of directional fading channels for millimeter wave systems," in *Proc. IEEE 86th Veh. Technol. Conf.*, pp. 1–5, Sep. 2017.

[13] J. Wang *et al.*, "Quasi-deterministic model for doppler spread in millimeter-wave communication systems," *IEEE Antennas Wireless Propag. Lett.*, vol. 16, pp. 2195–2198, 2017.

[14] R. Sun *et al.*, "Design and calibration of a double-directional 60 GHz channel sounder for multipath component tracking," in *Proc. IEEE Eur. Conf. Antennas Propag.*, Mar. 2017, pp. 1–5.

[15] IEEE P802.11 - Task Group ay, "Status of Project IEEE 802.11ay," 2014. [Online]. Available at: http://www.ieee802.org/11/Reports/tgay_update.htm

[16] *IEEE 802.11ay Use Cases*. IEEE Standard 802.11-2015/625, Sep. 2015.

[17] D. Halperin *et al.*, "Augmented data center networks with multi-gigabit wireless links," in *Proc. ACM SIGCOMM Conf.*, Aug. 2011, vol. 41, no. 4, pp. 38–29.

[18] X. Zhou *et al.*, "Mirror mirror on the ceiling: flexible wireless links for data centers," in *Proc. ACM SIGCOMM Conf.*, Sep. 2012, vol. 42, no. 4, pp. 443–454.

[19] M. Z. Zaaimia *et al.*, "60-GHz statistical channel characterization for wireless data centers," *IEEE Antennas Propag. Lett.*, vol. 15, pp. 976–979, 2016.

[20] P. B. Papazian *et al.*, "Radio channel sounder for mobile millimeter-wave communications," *IEEE Trans. Microw. Theory Techn.*, vol. 64, no. 9, pp. 2924–2932, Aug. 2016.

[21] J. Wang *et al.*, "Unsupervised clustering for millimeter-wave channel propagation modeling," in *Proc. IEEE Veh. Technol. Conf.*, Sep. 2017, pp. 1–4.

[22] P. B. Papazian *et al.*, "Calibration of millimeter-wave channel sounders for super-resolution multipath component extraction," in *Proc. IEEE Eur. Conf. Antennas Prop.*, Apr. 2016, pp. 1–5.

[23] G. D. Galdo, N. Czink, and C. Mecklenbrauker, "Cluster spatial localization from high-resolution parameter estimation," in *Proc. ITG Workshop Smart Antennas*, 2006, pp. 1–5.